Charge density waves and structural phase transition in the high-T_c superconducting LaH_{10} quantum crystal

Christian Tantardini,[1,*] Alexander G. Kvashnin,[2] Matteo Giantomassi,[3] Miroslav Iliaš,[4,5] Boris I. Yakobson,[6] Russell J. Hemley,[7,†] and Xavier Gonze[3,‡]

[1]*Center for Integrative Petroleum Research, King Fahd University of Petroleum and Minerals, Dhahran 31261, Saudi Arabia*
[2]*National University of Science and Technology MISiS, Leninskiy Prospekt 4, Moscow 119049, Russian Federation*
[3]*European Theoretical Spectroscopy Facility, Institute of Condensed Matter and Nanosciences, Université Catholique de Louvain, Chemin des Étoiles 8, B-1348 Louvain-la-Neuve, Belgium*
[4]*GSI Helmholtzzentrum für Schwerionenforschung GmbH, Planckstrasse 1, D-64291 Darmstadt, Germany*
[5]*Helmholtz-Institut Mainz, Johannes Gutenberg–Universität, 55099 Mainz, Germany*
[6]*Department of Materials Science and Nanoengineering, Rice University, 6100 Main Street, Houston, Texas 77005, USA*
[7]*Departments of Physics, Chemistry, and Earth and Environmental Sciences, University of Illinois, Chicago, Illinois 60607, USA*

(Received 15 June 2025; revised 20 August 2025; accepted 8 September 2025; published 29 September 2025)

Second-order phase transitions in metals are a longstanding question, often linked to charge-density waves, Peierls distortions, or Kohn anomalies in the phonon spectrum. Such a phase transition has recently been observed in cubic LaH_{10}, a material that exhibits superconductivity with exceptionally high critical temperature up to 260 K. Previous work has shown that this phase is unstable below 200 GPa if quantum effects and anharmonicity are not present. Here, we study the instabilities occurring in this material at such pressures. Lowering the *electronic temperature* to 0 K softens the phonon branches along the Γ-X, K-Γ, Γ-L-U, and W-L-K directions. We relate these softenings to the linewidths predicted in the electronic high-temperature phonon band structure of LaH_{10} at specific wave vectors. The correspondence is striking: both functions are either large or small for all investigated wave vectors. In contrast, the Fermi nesting function, often invoked for such structural phase transitions, provides little insight. The phase transition in LaH_{10} is found to be similar to the one previously observed for paradigmatic charge-density-wave materials, $2H$-$NbSe_2$, $TaTe_4$, and $1T$-VSe_2. Going beyond the observation of a simple coincidence between the softening and the linewidth, we highlight the similarities and differences between the equations describing the Fermi surface nesting function, the phonon linewidth, and the temperature dependence of the phonon frequencies. Furthermore, we analyze the contributions to the calculated phonon linewidth from the four electronic bands crossing the Fermi surface of LaH_{10}. One specific intra-band contribution clearly dominates. However, the corresponding variation in the charge density of that specific band with temperature is negligible.

DOI: 10.1103/c7w9-7tgy

I. INTRODUCTION

In his seminal work, Kohn [1] pointed out that the sharp change in electronic occupation at the Fermi energy in metals can qualitatively modify the phonon band structure at zero temperature. For three-dimensional (3D) periodic crystals, an infinite slope in the phonon frequency as a function of the wave vector normal to a surface inside the Brillouin zone is found. For one-dimensional (1D) solids, the same argument yields a logarithmic divergence in the phonon frequency at specific wave vectors [2,3]. This concept aligns with Peierls' argument that 1D metallic chains with a single atom per unit cell are intrinsically unstable and spontaneously dimerize [4]. Also, charge-density waves (CDWs) arise in many different materials, and their relation to Peierls distortion has been explored [5,6]. Most CDWs are observed for materials that are metallic above the critical temperature below which the CDW develops, and for which the CDW depends on the strength of the electron-phonon coupling on the Fermi surface.

Kohn anomalies have been reported in materials ranging from conventional [7] and unconventional 3D superconductors [8,9] to low-dimensional systems such as carbon nanotubes [10], graphene [11–13], graphite [14], 1D conductors [2], and Weyl semimetals [15,16]. Similarly, CDW order has been observed in many materials, including the transition-metal dichalcogenides $2H$-$NbSe_2$, $2H$-TaS_2, and $2H$-$TaSe_2$ [17–20], which exhibit intertwined CDW and superconducting phases. In high-T_c cuprates (unconventional superconductors), incommensurate CDW correlations have been directly observed and appear to compete with superconductivity [21,22]. Signatures of CDW order also emerge in carbon nanotubes, where one-dimensionality enhances fluctuations that can stabilize such phases [23]. In general, CDWs, Peierls distortions, and Kohn anomalies are hallmarks of 1D conductors, driven largely by strong Fermi surface nesting [5,24]. Graphene may exhibit CDW instabilities under specific conditions (e.g., doping or strain) [25], while graphite

*Contact author: christiantantardini@ymail.com
†Contact author: rhemley@uic.edu
‡Contact author: xavier.gonze@uclouvain.be

 ©2025 American Physical Society

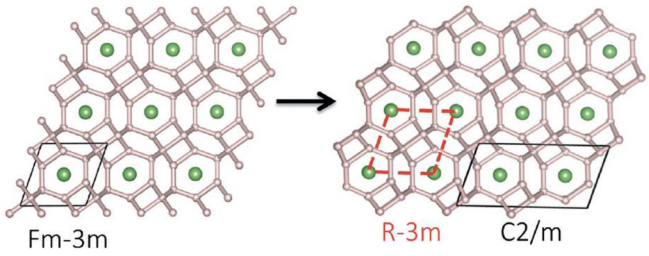

FIG. 1. LaH_{10} at 200 GPa, with primitive unit cells marked in black and the $R\bar{3}m$ primitive unit cell of the La sublattice marked in red. Optimization of the hydrogen positions gives a lower symmetry $C2/m$ structure (see Ref. [33]). Adapted from Ref. [33] with permission.

and its intercalation compounds show similar ordering due to electronic structure modifications [26]. More recently, CDW order has been observed at the surfaces of topological insulators, revealing novel phases formed by the interplay of topological surface states and interactions [27,28]. CDWs have also been identified in topological semimetals $SrAl_4$ and $EuAl_4$ [29], and theoretical work suggests that nesting between Weyl nodes in Weyl semimetals could induce related instabilities [30,31].

Among the newly discovered high-pressure superconductors, lanthanum decahydride (LaH_{10}) stands out, in view of its remarkably high superconductivity critical temperature near 260 K close to 200 GPa [32–42]. Its structure is intriguing, with lanthanum atoms sitting at the centers of 32 hydrogen atoms cages [32,33] (Fig. 1). The hydrogen-rich character of the material gives rise to pronounced quantum effects and strong anharmonicity.

Simulations show that these dynamical properties stabilize in LaH_{10} in its cubic $Fm\bar{3}m$ phase and lower the pressure at which the rhombohedral $R\bar{3}m$ phase emerges [32,37,40,41], in semiquantitative agreement with experiment [33,35,38]. However, the electronic origin of the phonon instability—and in particular the temperature dependence of the phonon softening—remains unclear.

Here we revisit the strong quantum-lattice character of $Fm\bar{3}m$ LaH_{10} at 200 GPa using first-principles calculations within DFT. We examine how the phonon band structure evolves with *electronic temperature*, from 0 K up to 4000 K using finite-temperature DFT with Fermi–Dirac occupations to account for electronic excitations [43]. By varying the electronic temperature in this way, we can track how the phonon band structure and any lattice instabilities evolve. We find that Fermi-surface nesting alone fails to pinpoint phonon instabilities. Instead, phonon linewidths, which are direct measure of electron-phonon coupling (EPC), identify the wave vectors and phonon branches that soften at lower temperatures. The EPC is dominated by intraband scattering from a single band with weak interband contributions. Real-space electron-density analyses and temperature-dependent Bader charges show that this band's charge remains nearly unchanged, revealing the carriers driving the phonon instability.

The reminder of the paper is as follows: Section II reviews our theoretical approach. In Sec. III we present the calculation of phonon dynamics of LaH_{10}. The electronic temperature dependence of the phonons is discussed in Sec. IV, followed by a detailed examination of the Fermi surface in Sec. VI. The overall results are discussed in Sec. VII. Section VIII details our computational method, including pseudopotential generation and the EPC formalism.

II. ELECTRON-PHONON COUPLING AND CHARGE-DENSITY WAVES

Within the Landau framework of second-order phase transitions [44–46], a CDW emerges below a critical temperature, spontaneously breaking the lattice's translational symmetry [4,47]. Above this temperature, an acoustic phonon branch typically softens at $\mathbf{q}_{\mathrm{CDW}}$. When related to a Kohn anomaly, segments of the Fermi surface become gapped [1]. In Weyl semimetals, $\mathbf{q}_{\mathrm{CDW}}$ can link distinct Weyl points and alter the system's topology [16]. In one dimension, the Peierls instability has $\mathbf{q}_{\mathrm{CDW}} = 2\mathbf{k}_F$ [4], whereas in three dimensions, Fermi surface nesting (FSN) can overcome the elastic cost of distortion, enabling the instability to form.

Despite extensive experimental study, the precise microscopic origins of these instabilities remain debated. While the notion of FSN explains acoustic-phonon softening in some systems, small deviations from perfect nesting can suppress the logarithmic divergence of the real part of the dielectric function, $\mathrm{Re}[\chi_q]$ [6]. Techniques such as angle-resolved photoemission spectroscopy, x-ray diffraction, and neutron diffraction repeatedly show limited FSN in materials that nevertheless form a CDW [48–53]. Consequently, alternative mechanisms must be examined.

In particular, strong electron-phonon coupling (EPC), where inelastic scattering between electrons and phonons is enhanced, can drive precursor features—such as phonon softening well above the transition temperature—that herald a CDW [54]. Its wave-vector dependence is also a crucial element, inducing softening in restricted parts of the Brillouin zone [55,56]. Indeed, inelastic x-ray scattering in $2H$-$NbSe_2$ showed in detail this phonon softening with temperature [19]. Recurrently, the relative contributions from FSN and from EPC have been described and debated [3,6,18,19,57–59].

Recently, phonon linewidths (which are inversely proportional to phonon lifetimes) have emerged as a crucial measure of EPC from states crossing the Fermi level [60] in relation to phonon instabilities [3,61,62]. The connection between the lifetime and temperature dependence of phonons has been observed, from experiment and first-principles simulations of $2H$-$NbSe_2$ [3,19]. The connection has also been pointed out for $TaTe_4$ [61] and for $1T$-VSe_2 [56], from first-principles simulations when varying the electronic temperature (i.e., that used in the Fermi-Dirac occupation function). Phonon softening becomes more pronounced as the electronic temperature drops, reflecting the change of Fermi-Dirac occupation near the Fermi surface. The same EPC near the Fermi level underlies Cooper pairing in superconductors, which is why structural phase transitions frequently appear in proximity to superconductivity [20,22].

The concept of an *electronic temperature* in DFT refers to how the electrons are thermally excited among the available energy levels, independent of the *ionic temperature* (which governs how strongly the ions themselves vibrate)

[34,63]. This approach is particularly useful for studying phenomena like Kohn anomalies, Peierls distortions, and charge-density waves, because all of these instabilities originate from the electronic structure—specifically, from how electrons near the Fermi level interact with phonons or with periodic modulations of the crystal lattice. By tuning the electronic temperature, one can observe how these instabilities weaken or disappear as electrons fill states above the Fermi level, thus preventing or delaying certain phase changes such as a Peierls distortion or eliminating a soft phonon mode associated with a CDW. Essentially, raising the electronic temperature washes out the sharp features at the Fermi level (where these instabilities arise), making it a direct tool to see how the system transitions from an unstable/ordered phase to a more stable/disordered phase.

III. LaH_{10} PHONON INSTABILITIES AND LINEWIDTHS

The phonon dispersion relations of $Fm\bar{3}m$-LaH_{10} at 200 GPa and 0 K are shown in Fig. 2(a). Acoustic phonon instabilities are seen along several directions, namely Γ-X, K-Γ, Γ-L-U. Also, there are instabilities for branches that cannot unambiguously be characterized as being acoustic branches, along W-L-K, or at the L-point [Fig. 2(a)], in agreement with Refs. [34,37]. To understand the origin of such instabilities, we have varied the *electronic temperature* at the level of Fermi-Dirac statistics within finite-temperature DFT [43,64]. At finite electronic temperature, the Fermi surface of the system is no longer a sharp feature in the Brillouin zone, and this has a direct impact on the stability of the crystal seen in the phonon band structure. The phonon band structure at 3000 K electronic temperature (0.26 eV) is shown in Fig. 2(b). The phonon instability at the L-point and along K-Γ, Γ-L-U, and W-L-K lines disappears. A subsequent increase of electronic temperature to 4000 K (0.34 eV) stabilizes the last acoustic phonon mode along $\Gamma-$X as well [see Fig. 2(c)]. Such phonon band structures at finite electronic temperature confirm that the quantum crystal nature of $Fm\bar{3}m$-LaH_{10} is linked to strong EPC at the Fermi surface. Although the presence of strong EPC is relatively easy to demonstrate by such (electronic) temperature-dependent phonon band structure, the origin of this dependence deserves more detailed study. Before discussing it, let us comment on the use of a high electronic temperature in DFT simulations. It might seem artificial to decouple the temperature of the ionic system from the temperature of the electronic system. Note, however, that heating suddenly the electronic system for a very short time before the ions have the time to react is made possible thanks to the use of ultrashort (femtosecond) laser pulses [65]. In such an experiment, the *ionic* and *electronic* temperatures can be decoupled. The goal is to establish a theoretical link between the wave vectors where phonons soften at low temperature and become unstable, and a simple indicator of the electron-phonon strength, still a function of the wave vector, namely the phonon lifetime due to EPC. The latter is well defined only if the phonon band structure is stable, hence justifying its computation for large electronic temperatures.

As mentioned in Sec. I, the simplest theoretical explanation for the appearance of charge-density waves invokes Fermi surface nesting [6]. Fermi surface nesting is also directly linked with Kohn anomalies. The Fermi surface nesting function, $\xi_{\mathbf{q}}$, which depends on the phonon wave vector $\mathbf{q}$, but not on the phonon branch ν, is defined [61] as

$$\xi_{\mathbf{q}} = \frac{n_s \Omega_0}{(2\pi)^3} \int_{\mathrm{BZ}} d^3\mathbf{k} \sum_{mn} \delta(\epsilon_{m\mathbf{k}+\mathbf{q}} - \epsilon_{\mathrm{F}}) \delta(\epsilon_{n\mathbf{k}} - \epsilon_{\mathrm{F}}). \quad (1)$$

The integral is over $\mathbf{k}$, the electronic wave vector in the Brillouin zone. The integrand, the product of two δ functions, is averaged, thanks to division by the volume of the Brillouin zone Ω_{BZ}, as $\Omega_{\mathrm{BZ}} = \frac{(2\pi)^3}{\Omega_0}$, where Ω_0 is the volume of the primitive cell. The factor $n_s = 2$ accounts for the spin. The

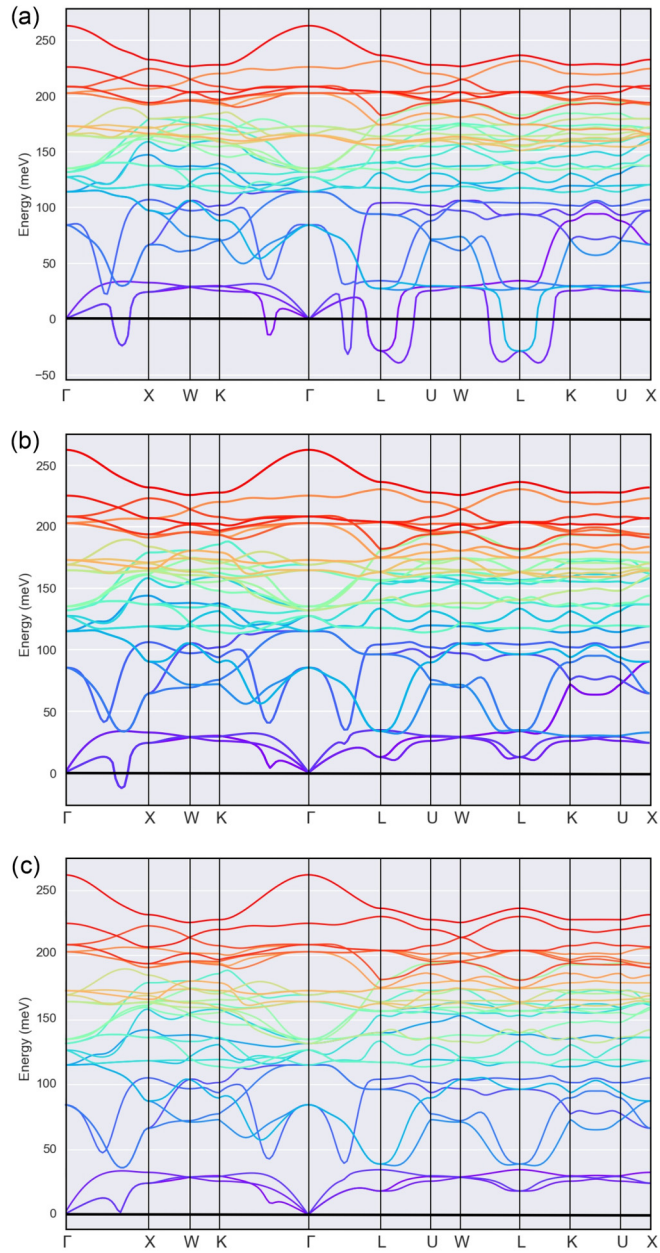

FIG. 2. Phonon band structure $Fm\bar{3}m$-LaH_{10} at electronic temperatures of 0 K (a), 3000 K (b), and 4000 K (c) (for each, the ionic temperature is set to 0 K). Imaginary phonon frequencies are represented as negative values. Colors track the phonon eigenvalues.

double summation over bands m and n only includes contributions where the energies of both bands, $\epsilon_{m\mathbf{k}+\mathbf{q}}$ and $\epsilon_{n\mathbf{k}}$, are equal to the Fermi energy ϵ_F. $\xi_{\mathbf{q}}$ does not contain any information about the electron-phonon coupling.

At variance, the phonon linewidth (or lifetime) [60] contains such information. When expressed in the adiabatic approximation and at $T = 0$ K, it reads

$$\gamma^{\mathrm{ad0}}_{\mathbf{q}\nu} = \frac{n_s \Omega_0 \omega_{\mathbf{q}\nu}}{(2\pi)^2} \int_{\mathrm{BZ}} d^3\mathbf{k} \sum_{mn} |g_{mn\nu}(\mathbf{k},\mathbf{q})|^2 \times \delta(\epsilon_{m\mathbf{k}+\mathbf{q}} - \epsilon_{\mathrm{F}})\delta(\epsilon_{n\mathbf{k}} - \epsilon_{\mathrm{F}}), \quad (2)$$

where $|g_{mn\nu}(\mathbf{k},\mathbf{q})|^2$ is the square of the EPC matrix element for each phonon mode, with frequency $\omega_{\mathbf{q}\nu}$ [66]. The similarity with Eq. (1) is striking: they differ from each other by the presence of the square of the electron-phonon matrix element, apart from a $2\pi\omega_{\mathbf{q}\nu}$ prefactor factor. The computation of $\gamma^{\mathrm{ad0}}_{\mathbf{q}\nu}$ is discussed in Sec. VIII B, also considering possible variations of Eq. (2).

Figure 3 presents the lowest (acoustic) part of the phonon band structure of $Fm\bar{3}m$-LaH_{10} at 4000 K (a), the changes of these phonon branches from 3000 to 4000 K (b), and (c) an evaluation of the second derivative of the square of the phonon frequencies at 0 K, from the fitting of our 0, 3000, and 4000 K data. The lowest phonon branch (transverse acoustic TA1) changes rapidly with the temperature at specific points, along Γ-X (about two-thirds along this line), along K-Γ (about one-half along that line), and also in a large neighborhood around L. The second transverse acoustic mode (TA2) is degenerate with TA1 along Γ-X and thus also changes rapidly in the same specific zone, and also changes rapidly around L, although the change decays faster away from L than for TA1. No rapid change is observed for TA2 along K-Γ. The longitudinal acoustic mode LA also exhibits some noticeable change with temperature, although less pronounced than for the TA1 and TA2 modes. Its relevance for the current analysis is not as high as that of the TA1 and TA2 modes, because it is higher in energy for most of the wave vectors. We will not comment further about it.

Figure 3(d) also shows the acoustic phonon linewidths. The correspondence with Figs. 3(b) and 3(c) is striking. Apart from a global scaling, the two functions depart from a negligible value in the same regions of the Brillouin zone, and for the same phonon branches. Thus the linewidth is indeed a good proxy for the rapid change of phonon frequencies with temperature. Hence they correlate with CDW formation. One can identify nevertheless that, close to Γ, some features of the linewidths are suppressed in the temperature difference or derivative plots in Figs. 3(b) and 3(c). Such a link between phonon lifetimes and their temperature dependence has been observed for $2H$-$NbSe_2$, in a joint experimental and theoretical work [19]. However, it had not been analyzed or explained further. For $TaTe_4$, presenting a charge-density-wave instability [61], the linewidth of the phonons had been studied, as well as the change of selected soft phonon frequencies with temperature, with also a similarity between these. In the search for an understanding of this correspondence between Figs. 3(b), 3(c), and 3(d), the study of the change of the phonon frequency with respect to the electronic temperature should be undertaken, as well as its dependence on the wave vector.

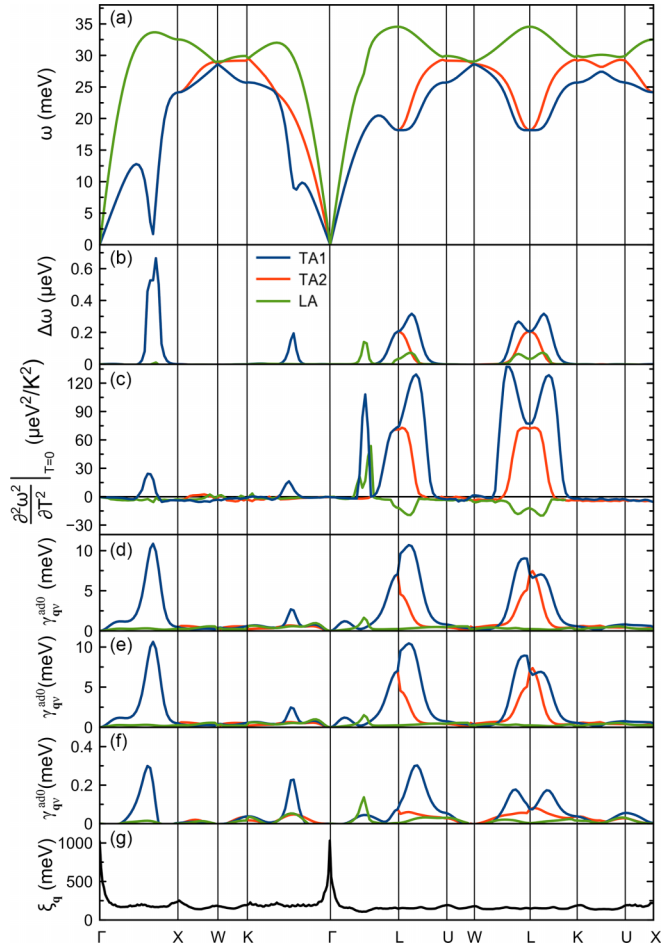

FIG. 3. The three acoustic phonon branches of $Fm\bar{3}m$-LaH_{10} at (a) 4000 K electronic temperature, and (b) the corresponding frequency change with electronic temperature from 3000 to 4000 K. (c) $\partial^2\omega^2/\partial T^2|_{T=0}$ for the fitting $\omega^2 = a + bT^2 + cT^4$ of data at 0, 3000, and 4000 K. Phonon linewidths at 4000 K electronic temperature: (d) total, (e) diagonal, (f) nondiagonal. (g) Fermi nesting function at 4000 K electronic temperature. Note the scale of the nondiagonal contribution to the (f) linewidth with respect to the (e) diagonal or (d) total linewidths.

IV. PHONON ELECTRONIC TEMPERATURE DEPENDENCE

We sketch here such a study, and the associated connection with the lifetime, while a more detailed investigation will be considered in a future publication [67]. Obviously, the correspondence that is found comparing Figs. 3(b), 3(c), and 3(d) is at best semiquantitative.

To establish a connection between Eq. (2) and the temperature dependence of the phonon frequencies, we first define

$$G_{\mathbf{q}\nu}(\varepsilon_{\mathrm{A}},\varepsilon_{\mathrm{B}}) = \frac{n_s\Omega_0}{(2\pi)^3} \int_{\mathrm{BZ}} d^3\mathbf{k} \sum_{mn\mathbf{k}} |g_{mn\nu}(\mathbf{k},\mathbf{q})|^2 \times (\delta(\varepsilon_{m\mathbf{k}+\mathbf{q}} - \varepsilon_{\mathrm{A}})\delta(\varepsilon_{n\mathbf{k}} - \varepsilon_{\mathrm{B}})), \quad (3)$$

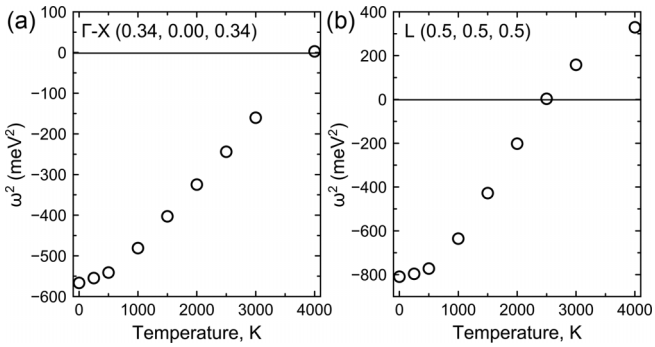

FIG. 4. Square of the phonon frequency (ω^2) as a function of electronic temperature for (a) the approximate minimum between Γ and X (0.34, 0.00, 0.34), and (b) the L point.

a symmetric function of its two arguments (ε_A, ε_B). This functions relate to $\gamma^{ad0}_{\mathbf{q}\nu}$ when considered at $\varepsilon_A = \varepsilon_B = \varepsilon_F$, namely

$$\gamma^{ad0}_{\mathbf{q}\nu} = 2\pi\omega_{\mathbf{q}\nu} G_{\mathbf{q}\nu}(\varepsilon_F, \varepsilon_F). \tag{4}$$

As sketched in Appendix B, the major contribution to the **q**-modulation of the temperature change of phonon frequencies is proportional to

$$(k_B T)^2 \int_{-\infty}^{+\infty} d\varepsilon_A \frac{\partial}{\partial \varepsilon_B}\left(\frac{G_{\mathbf{q}\nu}(\varepsilon_A, \varepsilon_B)}{\varepsilon_A - \varepsilon_B}\right)\Bigg|_{\varepsilon_B=\epsilon_F}. \tag{5}$$

One clearly sees that Eqs. (4) and (5) are not identical. However, they share the presence of the square of the EPC elements averaged over the Brillouin zone, for the specific $\mathbf{q}\nu$ phonon mode, through the $G_{\mathbf{q}\nu}$ function. They also share its evaluation at, or around, ε_F, at least for one argument in the case of Eq. (5). Thus, Eq. (4), the phonon linewidth, and Eq. (5), the rate of change of the phonon frequency with temperature, are theoretically linked as observed in Fig. 3.

By contrast, the FSN, represented in Fig. 3(f), and stemming from Eq. (1), does not show any correspondence with Figs. 3(b) and 3(c), stemming from Eq. (2). The role of the EPC is thus clearly apparent, as these two equations differ primarily by the absence or presence of the coupling.

On the other hand, examination of the temperature dependence of the phonon band structure at higher temperatures reveals that the square of phonon frequencies is not simply quadratic with respect to temperature. For the lowest frequency phonons at two representative specific q-vectors, the approximate minimum between Γ and X (0.34, 0.00, 0.34), and the L-point, the lowest-order quadratic behavior is smoothly superceded around 500 K by a linear behavior at higher temperatures (Fig. 4). Such a linear behavior can be represented by

$$\frac{\partial \omega^2_{\mathbf{q}\nu}(T)}{\partial T} = \lambda_{\mathbf{q}\nu} \tag{6}$$

from 1000 to 3000 K for these two modes, describing a linear softening of $\omega^2_{\mathbf{q}\nu}(T)$ with temperature.

From 3000 to 4000 K, the slope of the L-phonon frequency decreases [see Fig. 4(b)]. This change could imply that the available electronic states that contribute to the EPC start to impact in a similar way the second derivative of the free energy, whatever their energy. This phenomenon has a limited impact on the semiquantitative comparison between the phonon frequency changes with temperature and the phonon lifetime.

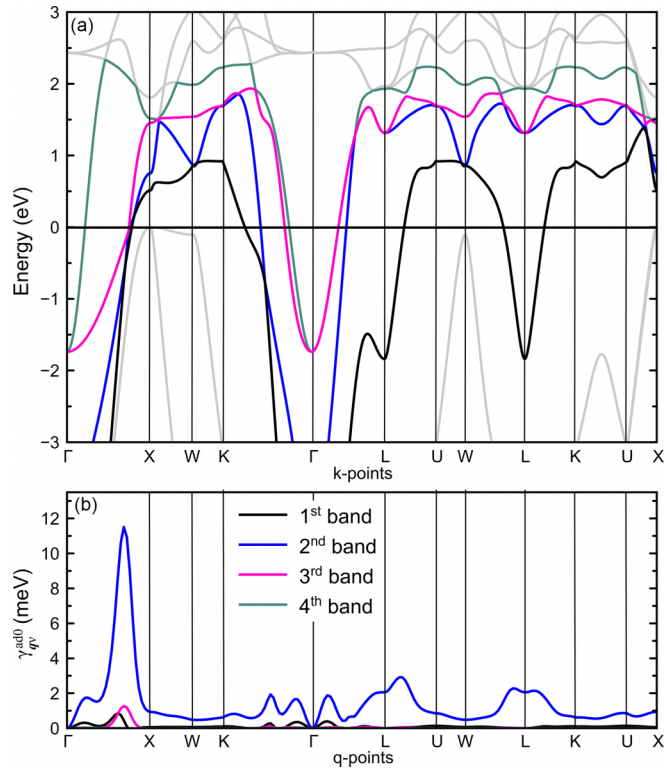

FIG. 5. (a) Electronic band structure and (b) decomposition of the phonon linewidth of the acoustic modes for the four bands crossing the Fermi surface. The fourth band has a phonon linewidth contribution of the order of 10^{-8} eV.

V. CONTRIBUTIONS TO THE PHONON LINEWIDTH

The phonon linewidth, Eq. (2), as a proxy for the location of the CDW wave vector can be analyzed further. This is possible through the disentangling of the diagonal contribution (i.e., intraband contribution), namely $m = n$ in Eq. (2), from the nondiagonal band contribution (i.e., interband contribution), namely $m \neq n$ in Eq. (2) [see Fig. 3(e)]. Although the characteristic features occur for the same wave vector and phonon branches, a difference of more than one order of magnitude between intraband and interband contributions in favor of the first ones is observed.

It is instructive to explore this large difference. One might argue that for the intraband term, the periodic parts of the left and right Bloch wave functions $u^{(0)}_n$ of such $n = m$ matrix elements, $g_{nn\nu}(\mathbf{k}, \mathbf{q})$ (i.e., diagonal electron-phonon matrix elements), are rather similar and interfere constructively, apart from a **q**-modulation, and the first-order change of external potential, also with **q**-modulation, couples well with such a **q**-modulated function.

Such an observation can further be combined with the necessary condition that a band must cross the Fermi energy to give a contribution to $\gamma^{ad0}_{\mathbf{q}\nu}$ [see Fig. 5(a)]. Only four bands cross the Fermi energy and contribute to the linewidth, and

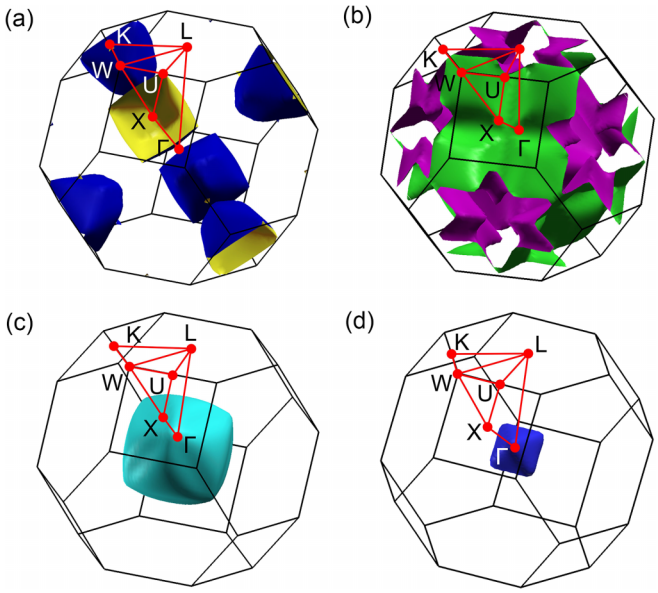

FIG. 6. (a) First, (b) second, (c) third, and (d) fourth electronic band structure Fermi surfaces within the Brillouin zone.

thus to the instabilities, thanks to their interaction with the acoustic phonons. The intraband contribution to the linewidth can further be obtained from each of these four bands crossing the Fermi surface, as shown in Fig. 5(b). The contribution from the second band completely dominates the linewidth.

VI. FERMI SURFACE

We represent the Fermi surfaces of the four bands in Fig. 6. While the Fermi surfaces for the first, third, and fourth bands are easily visualized, the Fermi surface of the second band is much more convoluted, although completely connected. The biggest contribution to the linewidths comes from the band that is most extended within the Brillouin zone. However, such a geometric effect cannot be the key explanation for the dominance of the second band, since we know that the FSN, in which such an effect is included, does not correlate with the linewidth.

Having singled out the major contribution from the second band, a further link with the CDW can be searched in real space. Indeed, the variation of the ground-state charge density $\Delta\rho(r)$ with temperature from 0 to 4000 K can now be studied, and decomposed in its contributions from the different bands, especially the first, second, and third bands represented in Fig. 5(a). Such a charge-density change must be indicative of the weakening/strengthening of the bonds, causing stabilization of the high-temperature phase. Such an analysis of charge density was performed thanks to Bader's theory [68] of partial atomic charges, and further decomposed in the contribution of each band to each atomic charge (see Table I and Fig. 7).

The two types of hydrogen atoms that are nonequivalent by symmetry are described in Table I and are represented in Fig. 7(a). The H1 atoms are the closest ones to the central lanthanum atom, while the H2 atoms are the farthest H atoms along the (111) direction. Although not fully occupied (as they cross the Fermi energy), the first three bands have a significant charge density, including around the lanthanum atom.

TABLE I. Bader charge contributions of atoms nonequivalent for symmetry within the unit cell to the bands that cross the Fermi surface (see Fig. 4) at 0 K and Δ from 0 to 4000 K.

Band	First	Second	Third	Fourth
La	0.329	0.239	0.033	0.000
Δ La	−0.004	0.002	0.003	0.000
H1	0.167	0.100	0.013	0.000
Δ H1	−0.002	0.000	0.000	0.000
H2	0.044	0.015	0.015	0.004
Δ H2	0.000	0.000	0.002	0.002
TOT	0.540	0.354	0.061	0.004
Δ TOT	−0.006	0.002	0.005	0.002

The projected density of states (pDOS) analysis reveals that these bands do not resemble the *f* or *d* orbitals of

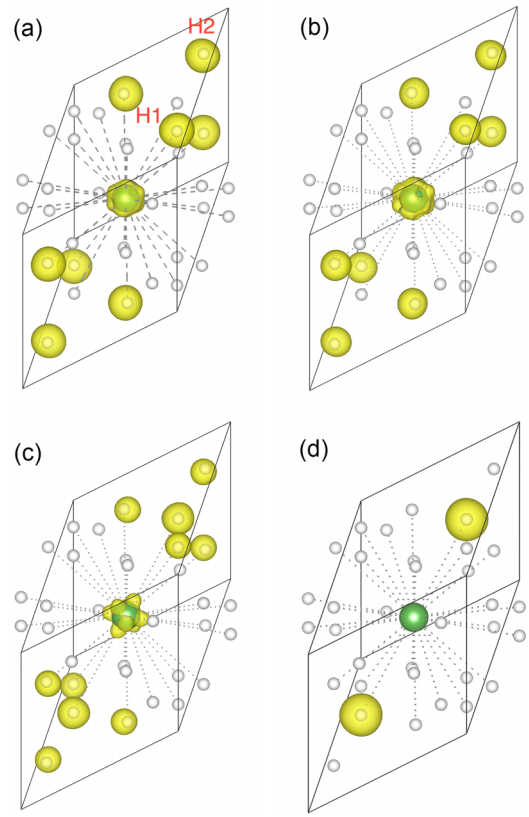

FIG. 7. Charge density in real space from the (a) first band, isosurface at 0.018 e/Bohr^3; (b) second band, isosurface at 0.011 e/Bohr^3; (c) third band, isosurface at 0.014 e/Bohr^3; and (d) fourth band, isosurface 0.0024 e/Bohr^3. These four electronic bands cross the Fermi surface. The lanthanum atom is at the center of the primitive cell. All the other atoms are hydrogen. The whole shell of H nearest neighbors to the central La atom (green) is represented, although for the sake of clarity, the charge density is represented only for the H atoms (white) that belong to the primitive cell. In (a) and (b) the charge density is localized on H atoms belonging to a cube of eight H atoms, while in (d) the H atoms are along the (111) direction. In (c) both types of atoms are contributing.

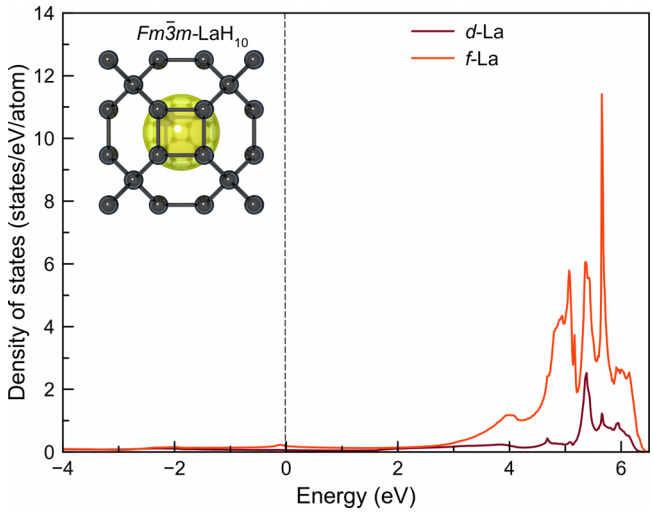

FIG. 8. Electron density of states for the *d*- and *f*-orbitals.

lanthanum, which are populated only at high energies, that primarily contribute to the conduction bands (see Fig. 8). At variance, the charge density at the fourth band is on the order of 10^{-2} e/Bohr^3 and contributes little around the lanthanum atom (see Table II). The contribution of the fourth band to $\gamma^{\mathrm{ad0}}_{\mathbf{q}\nu}$ (i.e., EPC) is indeed practically zero (see Fig. 5). The first and third bands exhibit similar but opposite variations in charge density with increasing temperature—a decrease of −0.02 for the first band and an increase of 0.01 for the third band—coupled with significant phonon linewidths. These bands appear to be the primary drivers of charge-density-wave (CDW) formation. In many established CDW systems, the temperature evolution of the charge-density modulation acts as an order parameter that directly signals the onset of the CDW state, while a broadened phonon linewidth indicates strong electron-phonon coupling, which is critical for stabilizing the CDW through lattice distortions [5,24]. In contrast, the absence of any temperature-dependent charge-density modulation in the second band, which contributes most significantly to $\gamma^{\mathrm{ad0}}_{\mathbf{q}\nu}$ (i.e., EPC), indicates that, for a band to drive a CDW, it must exhibit such modulation as the order parameter for the transition. Since this band does not show the necessary modulation, it cannot be responsible for CDW formation.

VII. DISCUSSION

We have revisited the $Fm\bar{3}m - R\bar{3}m$ transition in LaH_{10} quantum crystal that has previously been shown to arise from an instability driven by strong EPC [34]. We show that high electronic temperature stabilizes the high-symmetry structure, while instabilities develop when lowering the electronic temperature, precisely for the phonons that have the largest linewidth at high temperature. A similar correspondence had been seen previously for $2H$-$NbSe_2$ [3,19], $1T$-VSe_2 [56], and $TaTe_4$ [61], which are paradigmatic charge-density-wave materials. Moreover, we provide some theoretical analysis of this correspondence: a new function, which probes the integrated EPC strength at two different energies, is introduced. When considered at the Fermi energy, this function reduces to the phonon lifetime in the adiabatic approximation, apart from some prefactors. An integrated expression of this function yields an approximate measure of the quadratic change of phonon frequencies with temperature. Unlike the phonon linewidth, the Fermi surface nesting function does not correlate with the large temperature derivative of the phonon frequency. We demonstrate that the large phonon linewidths at the incipient CDW wave vectors arise from *intraband electronic scattering* within those bands that (i) cross the Fermi level and (ii) couple most strongly to the relevant acoustic phonons. In reciprocal space, the strongest linewidths coincide with the most extended and convoluted Fermi-surface sheets, yet a direct evaluation of the conventional nesting function shows no pronounced features—evidence that it is the EPC matrix elements, not simple nesting, that control the anomaly. A complementary real-space decomposition of the charge density reveals that the band supplying the dominant intraband contribution exhibits *negligible temperature-dependent charge modulation*; hence it drives EPC but not the CDW.

TABLE II. Atomic fractional coordinates and Bader charge contributions from the bands that cross the Fermi surface, which is shown in Fig. 5 at 0 K, 4000 K (†), and Δ from 0 to 4000 K.

Atom	x	y	z	First	Second	Third	Fourth	First †	Second †	Third †	Fourth †	First Δ	Second Δ	Third Δ	Fourth Δ
La	0.500	0.500	0.500	0.329	0.239	0.033	0.000	0.325	0.241	0.036	0.000	−0.004	0.002	0.003	0.000
H1	0.121	0.121	0.121	0.167	0.100	0.013	0.000	0.166	0.099	0.013	0.000	−0.002	0.000	0.000	0.000
H1	0.879	0.879	0.879	0.167	0.100	0.013	0.000	0.166	0.099	0.013	0.000	−0.002	0.000	0.000	0.000
H1	0.638	0.121	0.121	0.167	0.100	0.013	0.007	0.166	0.099	0.013	0.000	−0.002	0.000	0.000	-0.007
H1	0.362	0.879	0.879	0.167	0.100	0.013	0.000	0.166	0.099	0.013	0.011	−0.002	0.000	0.000	0.011
H1	0.121	0.638	0.121	0.167	0.100	0.013	0.000	0.166	0.099	0.013	0.000	−0.002	0.000	0.000	0.000
H1	0.879	0.362	0.879	0.167	0.100	0.013	0.000	0.166	0.099	0.013	0.000	−0.002	0.000	0.000	0.000
H1	0.121	0.121	0.638	0.167	0.100	0.013	0.000	0.166	0.099	0.013	0.000	−0.002	0.000	0.000	0.000
H1	0.879	0.879	0.362	0.167	0.100	0.013	0.000	0.166	0.099	0.013	0.000	−0.002	0.000	0.000	0.000
H2	0.250	0.250	0.250	0.044	0.015	0.015	0.004	0.044	0.015	0.018	0.006	0.000	0.000	0.002	0.002
H2	0.750	0.750	0.750	0.044	0.015	0.015	0.004	0.044	0.015	0.018	0.006	0.000	0.000	0.002	0.002
TOT				1.756	1.066	0.164	0.014	1.738	1.064	0.175	0.023	−0.018	−0.002	0.011	0.008

Notes: $a = 3.503$ Å for the optimized primitive cell of $Fm\bar{3}m$-LaH_{10} at 200 GPa and 0 K.

The combined reciprocal- and real-space workflow employed here—first stabilizing the translationally invariant phase at elevated electronic temperature and then analyzing phonon lifetimes/linewidths—should be broadly transferable. We recommend applying this protocol to other candidate CDW materials, including cage-type hydrides such as YH_{10} and ThH_{10}. We *predict* that the **q**-points with the shortest phonon lifetimes at high T_e will correlate with the soft-mode instabilities that emerge upon cooling, providing a practical first-principles route to identify CDW wave vectors in complex hydrides and beyond.

VIII. METHODS

A. Computational details

Plane-wave pseudopotential calculations were performed with the ABINIT code (version 9.6.2) [69–71], with the PBE exchange-correlation functional [72], lanthanum ONCVP (see the next subsection), and hydrogen ONCVP from the PseudoDojo project [73].

Lanthanum hydride (LaH_{10}) with space group $Fm\bar{3}m$ was optimized at 200 GPa. The plane-wave kinetic energy cutoff was 80 Ha with a Γ-centered $42 \times 42 \times 42$ **k**-point mesh within the full Brillouin zone. Such **k**-point mesh guarantees an energy convergence at the Γ-point of phonon optical modes on the order of 0.2%. The geometry optimization was obtained with the Broyden-Fletcher-Goldfarb-Shanno (BFGS) algorithm [74–77] with force tolerance for the maximum net force on atoms fixed at 5×10^{-5} Ha/Bohr.

The treatment of electronic temperature, with Fermi-Dirac occupations, relies on the double smearing scheme proposed in Ref. [43], further elaborated in Ref. [64]. In this scheme, the physical temperature is taken into account for the fermionic distribution function (we examined phonon band structures at 250, 500, 1000, 2000, 3000, and 4000 K electronic temperature), while an additional convolution with Gaussian smearing is applied, with smearing energy equal to 0.005 Ha. We tested smaller Gaussian smearing values of 0.003 and 0.001 Ha, requiring larger **k**-point meshes for convergence, but no significant modifications of the phonon band structures at fixed electronic temperature were observed.

Phonon band structures and phonon linewidths were calculated with variational density functional perturbation theory [64,78,79] (DFPT) using the same $42 \times 42 \times 42$ **k**-point mesh as for the ground state, and $6 \times 6 \times 6$ **q**-point mesh within the Brillouin zone. The convergence of the second derivative of the energy with respect to the atomic positions for each phonon mode was achieved when the tolerance on the potential residual was 10^{-8} Ha. Bader's analysis was performed using the CRITIC2 code [80,81].

B. Phonon linewidth

Parameters for the computation of phonon linewidths using Eq. (2) are presented in the previous subsection. In the present subsection, we discuss the very usage of Eq. (2) in our phonon linewidth computations. We emphasize that our approach aims at distinguishing the origin and type of the instabilities in LaH_{10}, and such a goal is conceptual, qualitative more than quantitative. Hence, the simplest is the most relevant.

A first delicate point relates to the use of two screened electron-phonon matrix elements in Eq. (2). Indeed, following the widespread procedure, the electron-phonon matrix elements in Eq. (2) are usually computed from the screened change of potential due to atomic displacements [82]. Theoretically, the combined use of screened and bare EPC elements, replacing $|g_{mn\nu}(\mathbf{k},\mathbf{q})|^2$ by $g^*_{mn\nu}(\mathbf{k},\mathbf{q})g^b_{mn\nu}(\mathbf{k},\mathbf{q})$, is better justified [66,83]. These two types of matrix elements are encountered in Eq. (B1). The potential change due to the phonon includes the Hartree and exchange-correlation response in the screened case, but not in the bare case. However, the difference is only second-order in the screening strength [83]. Additional considerations in favor of the use of two screened electron-phonon matrix elements can be found in Ref. [84]. On this basis, we prefer to use the simple formula Eq. (2).

A second point of discussion comes from the fact that, beyond the adiabatic approximation and for nonzero temperature, the phonon linewidth is obtained from the imaginary part of the phonon self-energy [60]. The Fermi golden rule gives the following formula:

$$\gamma_{\mathbf{q}\nu} = \frac{n_s \Omega_0}{(2\pi)^2} \int_{\mathrm{BZ}} d^3\mathbf{k} \sum_{mn} |g_{mn\nu}(\mathbf{k},\mathbf{q})|^2 (f_{m\mathbf{k}+\mathbf{q}} - f_{n\mathbf{k}}) \delta(\omega_{\mathbf{q}\nu} - \epsilon_{m\mathbf{k}+\mathbf{q}} + \epsilon_{n\mathbf{k}}). \quad (7)$$

However, Eq. (7) reduces to Eq. (2) for vanishing electronic temperature and in the adiabatic approximation, where the phonon frequencies are considered small with respect to electronic energy differences. The adequacy of this approximation was emphasized in Ref. [60]. In the context of the present work, we note that 4000 K corresponds to 0.34 eV, an energy for which the qualitative relevant features in the band structure, namely the dispersion of the bands around the Fermi level, are still the same as at 0 K. Also, the largest phonon energies are lower than 0.3 eV.

A third consideration comes from the fact that in the present work, $\gamma^{\mathrm{ad0}}_{\mathbf{q}\nu}$ from Eq. (2) is computed with the phonon frequencies at 4000 K. In principle, the formalism of EPC allows the calculations only for real phonon modes [66]. However, we note that the EPC matrix elements themselves include an inverse square root of the phonon frequencies; see Eqs. (21), (34), and (38) of Ref. [66]. The phonon frequencies present in the prefactor of Eq. (2) are thus canceled by those present in the EPC matrix elements. Indeed, the final result for $\gamma^{\mathrm{ad0}}_{\mathbf{q}\nu}$ depends on the phonon eigendisplacements and the associated change of potential, but not on the phonon eigenfrequencies. One might thus apply Eq. (2) even in the case of unstable phonon modes, although we have not attempted to do so.

For the purpose of the analysis of the role of the electron-phonon coupling, in comparison with the Fermi surface nesting [Eq. (2)], we will stick to the comparison between Eqs. (2) and (1) instead of using Eq. (7). Indeed, our approach aims at distinguishing the origin and type of the instabilities in LaH_{10}, and such a goal is conceptual, qualitative more than quantitative.

C. Pseudopotential development

To describe the electronic structure and electron-phonon interactions of $Fm\bar{3}m$-LaH_{10} at high pressure, we developed a scalar-relativistic, PBE-based optimized norm-conserving Vanderbilt pseudopotential (ONCVP) [85,86] for lanthanum. A small cutoff radius was chosen to mitigate overlap of pseudopotential spheres under compression, and the valence shell includes an empty 4*f* orbital to capture any 4*f*-orbital effects. We validated this pseudopotential against all-electron (AE) calculations employing the zeroth-order regular relativistic approximation (ZORA) [87–90], using the Δ-Gauge [91] as a quantitative measure of how closely both approaches reproduce the same energy landscape.

We constructed the ONCVP for lanthanum with 29 valence electrons ($4s^2 4p^6 4d^{10} 4f^{0.10} 5s^2 5p^6 5d^1 6s^{1.90}$) using the ONCVPSP code (version 4.0.1) [85,86,92]. Its performance was compared against AE calculations carried out with the BAND module of the Amsterdam Modeling Suite [93] and plane-wave (PW) calculations using ABINIT (version 9.6.2) [69–71]. Specifically, we computed the third-order Birch-Murnaghan equation of state for a face-centered-cubic (fcc) phase.

In the AE calculations, we employed a triple-ζ plus double-polarization basis set and optimized the geometry using the BFGS algorithm [74–77]. A Γ-centered $15 \times 15 \times 15$ **k**-point grid sampled the Brillouin zone, with a force-convergence criterion of 10^{-6} Ha/Bohr. Collinear magnetism was permitted along the *z*-direction, while spin-orbit coupling was neglected. The PW calculations employed the same parameters, an 80 Ha kinetic-energy cutoff, and a 0.001 Ha Fermi-Dirac smearing.

We found that the optimized lattice parameters differ by only 0.19% between our pseudopotential-based PW calculations and the ZORA-based AE calculations, while the Δ-Gauge was 0.18 meV/at. Since a Δ-Gauge below 1 meV/at indicates excellent agreement [91], this confirms the reliability of our ONCVP for lanthanum. For an element *i*, the Δ-Gauge between methods *a* (reference) and *b* is defined as

$$\Delta_i(a,b) = \sqrt{\frac{\int_{0.94V_{0,i}}^{1.06V_{0,i}} \left(E_{b,i}(V) - E_{a,i}(V)\right)^2 dV}{0.12\, V_{0,i}}}, \qquad (8)$$

where $E_{a,i}(V)$ and $E_{b,i}(V)$ are the respective equations of state, and $V_{0,i}$ is the equilibrium volume from method *a*. The smaller $\Delta_i(a,b)$ is, the more closely the two approaches predict the same energy landscape.

ACKNOWLEDGMENTS

This work was supported by the Fonds de la Recherche Scientifique (FRS-FNRS Belgium) through the PdR Grant No. T.0103.19 – ALPS, NSF (DMR-2104881) and DOE-NNSA (DE-NA 0004153). The calculations were performed at NOTUR – The Norwegian Metacenter for Computational Science through a grant of computer time (nn14654k). B.I.Y. was supported by the US Department of Energy BES Grant No. DE-2801 SC0012547.

DATA AVAILABILITY

The data that support the findings of this article are not publicly available upon publication because it is not technically feasible and/or the cost of preparing, depositing, and hosting the data would be prohibitive within the terms of this research project. The data are available from the authors upon reasonable request.

APPENDIX A: PROJECTED DENSITY OF STATES AND BADER CHARGES

In this Appendix, we present the electronic density of states for the *d*- and *f*-orbitals, (see Fig. 8), as well as Table II, with Bader charge contributions from the bands that cross the Fermi surface, at different electronic temperatures. The observation that the *d* and *f* orbital populations in LaH_{10} appear only at high energies—from 4 to 6 eV—suggests that these orbitals are not actively involved in the low-energy electronic processes near the Fermi level, where superconductivity typically emerges. This high-energy placement means that the *d* and *f* states are likely more localized and less hybridized with the conduction states responsible for electron transport and pairing. Consequently, the superconducting behavior of LaH_{10} is probably dominated by other orbitals, such as those associated with hydrogen or more delocalized La states, that reside closer to the Fermi level. The separation of these orbital contributions implies a clear distinction between the roles of high-energy, localized states and the low-energy, itinerant states crucial for electron-phonon interactions. Overall, this indicates that while the *d* and *f* orbitals are present in the material's electronic structure, their impact on superconductivity is minimal due to their energetic distance from the region where conduction and pairing occur.

APPENDIX B: THE SECOND-ORDER CHANGE OF FREE ENERGY AND ITS TEMPERATURE DEPENDENCE

In this Appendix, we sketch the study of the temperature dependence of the second-order free energy, in view of showing the connection between the electronic temperature dependence of phonon frequencies with their phonon lifetime. A more detailed analysis will be considered in a future publication [67]. The argument relies in part on well-established results from density functional perturbation theory [64,78].

The second-order change of free energy due to a collective atomic displacement (the phonon eigenvector) is linked to the square of the phonon frequency $\omega^2_{\mathbf{q}\nu}$ [64,78]. This change of free energy is decomposed in three contributions: (a) a first-order electronic response to the perturbation, combined with a first-order potential change, also due to the perturbation (nonfrozen contribution), (b) a second-order potential change due to the perturbation, with frozen electronic states, and (c) a second-order nonelectronic response (from bare ion-ion interactions). Referring to Eq. (14) of Ref. [78], (a) and (b) constitute $\tilde{C}_{\mathrm{el}}$, while (c) constitutes $\tilde{C}_{\mathrm{Ew}}$. Contribution (b) is Eq. (6) of the same paper.

The bare ion-ion interaction (a) does not depend on the electronic temperature, hence it can be ignored in the present analysis. The frozen electronic state contribution (b) depends on the electronic temperature. This dependence is smooth, coming from the change of occupation numbers of wave functions. However, it does not depend on the phonon wave vector, as seen in Eq. (49) of Ref. [78]. Hence, its role is not dominant

in the strongly varying features seen in Fig. 3(b). Hence, one can focus on the nonfrozen contribution (a). Its nonvariational expression, in notations close to Ref. [64], is

$$F^{(2)}_{\mathrm{nfr},-\mathbf{q},\mathbf{q}} = \frac{n_s\Omega_0}{2}\int_{\mathrm{BZ}}\sum_{mn}\frac{f^{(0)}_{m\mathbf{k}+\mathbf{q}}-f^{(0)}_{n\mathbf{k}}}{\varepsilon^{(0)}_{m\mathbf{k}+\mathbf{q}}-\varepsilon^{(0)}_{n\mathbf{k}}}\langle u^{(0)}_{n\mathbf{k}}|\hat{H}^{(1)}_{\mathbf{k},\mathbf{k}+\mathbf{q}}|u^{(0)}_{m\mathbf{k}+\mathbf{q}}\rangle \times\langle u^{(0)}_{m\mathbf{k}+\mathbf{q}}|\hat{v}^{(1)}_{\mathrm{ext},\mathbf{k}+\mathbf{q},\mathbf{k}}|u^{(0)}_{n\mathbf{k}}\rangle. \quad \text{(B1)}$$

In this equation, the two matrix elements correspond to screened and bare electron-phonon interaction, respectively. The difference between these can be ignored at the sought-after level of analysis, as in Eq. (2). The occupation numbers $f^{(0)}$ are given by Fermi-Dirac statistics, see Eqs. (13) and (14) of Ref. [64]:

$$f^{(0)}_{n\mathbf{k}} = f_{\mathrm{FD}}\left(\frac{\mu-\varepsilon^{(0)}_{n\mathbf{k}}}{k_{\mathrm{B}}T}\right), \quad \text{(B2)}$$

$$f_{\mathrm{FD}}(x) = [\exp(-x)+1]^{-1}, \quad \text{(B3)}$$

where $\varepsilon^{(0)}_{n\mathbf{k}}$ are the electronic eigenenergies. The chemical potential at $T = 0$ K becomes ϵ_{F}.

The temperature dependence of $F^{(2)}_{\mathrm{nfr},-\mathbf{q},\mathbf{q}}$ comes mainly from the Fermi-Dirac statistics, Eq. (B2), although there is an additional weak, indirect, dependence from the screening, affecting wave functions, eigenenergies, and screened EPC matrix element in Eq. (B1). These indirect dependences will be ignored.

The Sommerfeld expansion is a mathematical technique to obtain the low-temperature Taylor expansion of an integral in which a Fermi-Dirac function is present and from which the integral acquires an electronic temperature dependence. The main result, see Eq. (26a) of Ref. [94], is

$$I = \int_{-\infty}^{\infty} f_{\mathrm{FD}}\left(\frac{\mu-\varepsilon}{k_{\mathrm{B}}T}\right)h(\varepsilon)d\varepsilon = \int_{-\infty}^{\mu} h(\varepsilon)d\varepsilon + \frac{\pi^2}{6}h'(\mu)(k_{\mathrm{B}}T)^2 + O(k_{\mathrm{B}}T)^4, \quad \text{(B4)}$$

where $h'(\mu)$ denotes the derivative of the h function with respect to ε evaluated at μ. This result is valid provided that the h function is derivable twice. Using the function $G_{\mathbf{q}\nu}(\varepsilon_{\mathrm{A}},\varepsilon_{\mathrm{B}})$, defined in the main text, one sees that, setting aside prefactors, and given the above-mentioned approximations, the major contribution to the quadratic change of $F^{(2)}_{\mathrm{nfr},-\mathbf{q},\mathbf{q}}$ due to temperature, in a low-temperature expansion, denoted $\Delta F^{(2)}_{\mathrm{nfr},\mathbf{q}\nu}(T)$, is proportional to

$$\Delta F^{(2)}_{\mathrm{nfr},\mathbf{q}\nu}(T) \propto (k_{\mathrm{B}}T)^2\int_{-\infty}^{+\infty} d\varepsilon_{\mathrm{A}}\frac{\partial}{\partial\varepsilon_{\mathrm{B}}}\left(\frac{G_{\mathbf{q}\nu}(\varepsilon_{\mathrm{A}},\varepsilon_{\mathrm{B}})}{\varepsilon_{\mathrm{A}}-\varepsilon_{\mathrm{B}}}\right)\Bigg|_{\varepsilon_{\mathrm{B}}=\epsilon_{\mathrm{F}}}. \quad \text{(B5)}$$

Special care must be taken to deal with the discontinuities of $G_{\mathbf{q}\nu}(\varepsilon_{\mathrm{A}},\varepsilon_{\mathrm{B}})$ at the band edges.

[1] W. Kohn, Image of the Fermi surface in the vibration spectrum of a metal, Phys. Rev. Lett. **2**, 393 (1959).

[2] B. Renker, H. Rietschel, L. Pintschovius, W. Gläser, P. Brüesch, D. Kuse, and M. J. Rice, Observation of giant Kohn anomaly in the one-dimensional conductor $K_2Pt(Cn)_4Br_{0.3}\cdot 3H_2O$, Phys. Rev. Lett. **30**, 1144 (1973).

[3] X. Zhu, Y. Cao, J. Zhang, E. W. Plummer, and J. Guoa, Classification of charge density waves based on their nature, Proc. Natl. Acad. Sci. USA **112**, 2367 (2015).

[4] R. E. Peierls, *Quantum Theory of Solids* (Clarendon, Oxford, 1955).

[5] G. Grüner, The dynamics of charge-density waves, Rev. Mod. Phys. **60**, 1129 (1988).

[6] M. D. Johannes and I. I. Mazin, Fermi surface nesting and the origin of charge density waves in metals, Phys. Rev. B **77**, 165135 (2008).

[7] P. Aynajian, T. Keller, L. Boeri, S. M. Shapiro, K. Habicht, and B. Keimer, Energy gaps and Kohn anomalies in elemental superconductors, Science **319**, 1509 (2008).

[8] W. Weber, Electron-phonon interaction in the new superconductors $La_{2-x}(Ba,Sr)_xCuO_4$, Phys. Rev. Lett. **58**, 1371 (1987).

[9] D. Reznik, L. Pintschovius, M. Ito, S. Iikubo, M. Sato, H. Goka, M. Fujita, K. Yamada, G. D. Gu, and J. M. Tranquada, Electron-phonon coupling reflecting dynamic charge inhomogeneity in copper oxide superconductors, Nature (London) **440**, 1170 (2006).

[10] S. Piscanec, M. Lazzeri, J. Robertson, A. C. Ferrari, and F. Mauri, Optical phonons in carbon nanotubes: Kohn anomalies, Peierls distortions, and dynamic effects, Phys. Rev. B **75**, 035427 (2007).

[11] D. L. Mafra, L. M. Malard, S. K. Doorn, H. Htoon, J. Nilsson, A. H. Castro Neto, and M. A. Pimenta, Observation of the Kohn anomaly near the K point of bilayer graphene, Phys. Rev. B **80**, 241414(R) (2009).

[12] W.-K. Tse, B. Y.-K. Hu, and S. Das Sarma, Chirality-induced dynamic Kohn anomalies in graphene, Phys. Rev. Lett. **101**, 066401 (2008).

[13] B. Wunsch, T. Stauber, F. Sols, and F. Guinea, Dynamical polarization of graphene at finite doping, New J. Phys. **8**, 318 (2006).

[14] A. C. Ferrari, Raman spectroscopy of graphene and graphite: Disorder, electron–phonon coupling, doping and nonadiabatic effects, Solid State Commun. **143**, 47 (2007).

[15] S. Y. Xu, I. Belopolski, N. Alidoust, M. Neupane, G. Bian, C. Zhang, R. Sankar, G. Chang, Z. Yuan, C. C. Lee, S. M. Huang, H. Zheng, J. Ma, D. S. Sanchez, B. Wang, A. Bansil, F. Chou, P. P. Shibayev, H. Lin, S. Jia *et al.*, Discovery of a Weyl fermion semimetal and topological Fermi arcs, Science **349**, 613 (2015).

[16] T. Nguyen, F. Han, N. Andrejevic, R. Pablo-Pedro, A. Apte, Y. Tsurimaki, Z. Ding, K. Zhang, A. Alatas, E. E. Alp, S. Chi, J. Fernandez-Baca, M. Matsuda, D. A. Tennant, Y. Zhao, Z. Xu, J. W. Lynn, S. Huang, and M. Li, Topological singularity induced chiral Kohn anomaly in a Weyl semimetal, Phys. Rev. Lett. **124**, 236401 (2020).

[17] J. A. Wilson, F. J. Di Salvo, and S. Mahajan, Charge-density waves and superlattices in the metallic layered transition metal dichalcogenides, Adv. Phys. **24**, 117 (1975).

[18] K. Rossnagel, On the origin of charge-density waves in select layered transition-metal dichalcogenides, J. Phys.: Condens. Matter **23**, 213001 (2011).

[19] F. Weber, S. Rosenkranz, J.-P. Castellan, R. Osborn, R. Hott, R. Heid, K.-P. Bohnen, T. Egami, A. H. Said, and D. Reznik, Extended phonon collapse and the origin of the charge-density-wave in 2*H*-$NbSe_2$, Phys. Rev. Lett. **107**, 107403 (2011).

[20] H. M. Hill, S. Chowdhury, J. R. Simpson, A. F. Rigosi, D. B. Newell, H. Berger, F. Tavazza, and A. R. H. Walker, Phonon origin and lattice evolution in charge density wave states, Phys. Rev. B **99**, 174110 (2019).

[21] G. Ghiringhelli, M. Le Tacon, M. Minola, S. Blanco-Canosa, C. Mazzoli, N. B. Brookes, G. M. De Luca, A. Frano, D. G. Hawthorn, F. He *et al.*, Long-range incommensurate charge fluctuations in (Y,Nd)$Ba_2Cu_3O_{6+x}$, Science **337**, 821 (2012).

[22] J. Chang, E. Blackburn, A. T. Holmes, N. B. Christensen, J. Larsen, J. Mesot, R. Liang, D. A. Bonn, W. N. Hardy, A. Watenphul *et al.*, Direct observation of competition between superconductivity and charge density wave order in $YBa_2Cu_3O_{6.67}$, Nat. Phys. **8**, 871 (2012).

[23] D. A. Bagrets, Full current statistics of incoherent "cold electrons," Phys. Rev. Lett. **93**, 236803 (2004).

[24] P. Monceau, Electronic crystals: An experimental overview, Adv. Phys. **61**, 325 (2012).

[25] S. Chowdhury, A. F. Rigosi, H. M. Hill, P. Vora, A. R. H. Walker, and F. Tavazza, Computational methods for charge density waves in 2D materials, Nanomaterials **12**, 504 (2022).

[26] J. L. McChesney, A. Bostwick, T. Ohta, T. Seyller, K. Horn, J. González, and E. Rotenberg, Extended van Hove singularity and a potential charge-density-wave instability in graphite, Phys. Rev. Lett. **104**, 136803 (2010).

[27] F. Zangeneh-Nejad, A. Alù, and R. Fleury, Topological wave insulators: a review, C. R. Phys. **21**, 467 (2020).

[28] M. H. Fischer, A. Vaezi, A. Manchon, and E.-A. Kim, Spin-torque generation in topological insulator based heterostructures, Phys. Rev. B **93**, 125303 (2016).

[29] L.-L. Wang, N. K. Nepal, and P. C. Canfield, Origin of charge density wave in topological semimetals $SrAl_4$ and $EuAl_4$, Commun. Phys. **7**, 111 (2024).

[30] P. Hosur, S. A. Parameswaran, and A. Vishwanath, Charge transport in Weyl semimetals, Phys. Rev. Lett. **108**, 046602 (2012).

[31] A. A. Zyuzin, S. Wu, and A. A. Burkov, Weyl semimetal with broken time reversal and inversion symmetries, Phys. Rev. B **85**, 165110 (2012).

[32] H. Liu, I. I. Naumov, R. Hoffmann, N. W. Ashcroft, and R. J. Hemley, Potential high-T_c superconducting lanthanum and yttrium hydrides at high pressure, Proc. Natl. Acad. Sci. USA **114**, 6990 (2017).

[33] Z. M. Geballe, H. Liu, A. K. Mishra, M. Ahart, M. Somayazulu, Y. Meng, M. Baldini, and R. J. Hemley, Synthesis and stability of lanthanum superhydrides, Angew. Chem., Int. Ed. **57**, 688 (2018).

[34] H. Liu, I. I. Naumov, Z. M. Geballe, M. Somayazulu, J. S. Tse, and R. J. Hemley, Dynamics and superconductivity in compressed lanthanum superhydride, Phys. Rev. B **98**, 100102(R) (2018).

[35] M. Somayazulu, M. Ahart, A. K. Mishra, Z. M. Geballe, M. Baldini, Y. Meng, V. V. Struzhkin, and R. J. Hemley, Evidence for superconductivity above 260 K in lanthanum superhydride at megabar pressures, Phys. Rev. Lett. **122**, 027001 (2019).

[36] A. P. Drozdov, P. P. Kong, V. S. Minkov, S. P. Besedin, M. A. Kuzovnikov, S. Mozaffari, L. Balicas, F. F. Balakirev, D. E. Graf, V. B. Prakapenka, E. Greenberg, D. A. Knyazev, M. Tkacz, and M. I. Eremets, Superconductivity at 250 K in lanthanum hydride under high pressures, Nature (London) **569**, 528 (2019).

[37] I. Errea, F. Belli, L. Monacelli, A. Sanna, T. Koretsune, T. Tadano, R. Bianco, M. Calandra, R. Arita, F. Mauri, and J. A. Flores-Livas, Quantum crystal structure in the 250-kelvin superconducting lanthanum hydride, Nature (London) **578**, 66 (2020).

[38] D. Sun, V. S. Minkov, S. Mozaffari, Y. Sun, Y. Ma, S. Chariton, V. B. Prakapenka, M. I. Eremets, L. Balicas, and F. F. Balakirev, High-temperature superconductivity on the verge of a structural instability in lanthanum superhydride, Nat. Commun. **12**, 6863 (2021).

[39] A. K. Verma, P. Modak, F. Schrodi, A. Aperis, and P. M. Oppeneer, Prediction of an unusual trigonal phase of superconducting LaH_{10} stable at high pressures, Phys. Rev. B **104**, 174506 (2021).

[40] I. Errea, Superconducting hydrides on a quantum landscape, J. Phys.: Condens. Matter **34**, 231501 (2022).

[41] K. K. Ly and D. M. Ceperley, Stability and distortion of fcc LaH_{10} with path-integral molecular dynamics, Phys. Rev. B **106**, 054106 (2022).

[42] C. Xie, A. D. Smith, H. Yan, W.-C. Chen, and Y. Wang, Dynamical approach to realize room-temperature superconductivity in LaH_{10}, npj Comput. Mater. **11**, 227 (2025).

[43] M. Verstraete and X. Gonze, Smearing scheme for finite-temperature electronic-structure calculations, Phys. Rev. B **65**, 035111 (2001).

[44] L. D. Landau, On the theory of phase transitions, Zh. Eksp. Teor. Fiz. **7**, 19 (1937).

[45] L. D. Landau, On the theory of phase transitions. II, Zh. Eksp. Teor. Fiz. **7**, 627635 (1937).

[46] L. D. Landau and E. M. Lifshitz, *Statistical Physics, Part 1*, 3rd ed., Course of Theoretical Physics (Pergamon, Oxford, 1980), Vol. 5, p. 384.

[47] H. Fröhlich, On the theory of superconductivity: the one-dimensional case, Proc. R. Soc. London, Ser. A **223**, 296 (1954).

[48] D. S. Inosov, V. B. Zabolotnyy, D. V. Evtushinsky, A. A. Kordyuk, B. Büchner, R. Follath, H. Berger, and S. V. Borisenko, Fermi surface nesting in several transition metal dichalcogenides, New J. Phys. **10**, 125027 (2008).

[49] S. V. Borisenko, A. A. Kordyuk, V. B. Zabolotnyy, D. S. Inosov, D. Evtushinsky, B. Büchner, A. N. Yaresko, A. Varykhalov, R. Follath, W. Eberhardt, L. Patthey, and H. Berger, Two energy gaps and Fermi-surface "arcs" in $NbSe_2$, Phys. Rev. Lett. **102**, 166402 (2009).

[50] O. Singh and A. E. Curzon, An electron diffraction evidence of charge density wave instability in 2*H*-$NbSe_2$, Phys. Lett. A **56**, 63 (1976).

[51] C. H. Chen, Electron diffraction study of the charge-density wave superlattice in 2*H*-$NbSe_2$, Solid State Commun. **49**, 645 (1984).

[52] D. E. Moncton, J. D. Axe, and F. J. DiSalvo, Study of superlattice formation in $2H$-$NbSe_2$ and $2H$-$TaSe_2$ by neutron scattering, Phys. Rev. Lett. **34**, 734 (1975).

[53] D. E. Moncton, J. D. Axe, and F. J. DiSalvo, Neutron scattering study of the charge-density wave transitions in $2H-TaSe_2$ and $2H-NbSe_2$, Phys. Rev. B **16**, 801 (1977).

[54] S.-K. Chan and V. Heine, Spin density wave and soft phonon mode from nesting Fermi surfaces, J. Phys. F **3**, 795 (1973).

[55] J.-P. Pouget, E. Canadell, and B. Guster, Momentum-dependent electron-phonon coupling in charge density wave systems, Phys. Rev. B **103**, 115135 (2021).

[56] J. Diego, D. Subires, A. H. Said, D. A. Chaney, A. Korshunov, G. Garbarino, F. Diekmann, S. K. Mahatha, V. Pardo, J. M. Wilkinson, J. S. Lord, J. Strempfer, P. J. B. Perez, S. Francoual, C. Popescu, M. Tallarida, J. D. Raffaello Bianco, L. Monacelli, M. Calandra, A. Bosak *et al.*, Electronic structure and lattice dynamics of $1T$-VSe_2: Origin of the three-dimensional charge density wave, Phys. Rev. B **109**, 035133 (2024).

[57] D. Pasquier and O. V. Yazyev, Unified picture of lattice instabilities in metallic transition metal dichalcogenides, Phys. Rev. B **100**, 201103(R) (2019).

[58] Z. Wang, C. Chen, J. Mo, J. Zhou, K. P. Loh, and Y. P. Feng, Decisive role of electron-phonon coupling for phonon and electron instabilities in transition metal dichalcogenides, Phys. Rev. Res. **5**, 013218 (2023).

[59] Y.-T. Lee, P.-T. Chen, Z.-H. Li, J.-Y. Wu, C.-N. Kuo, C. S. Lue, C.-T. Wu, C.-C. Kuo, C.-T. Chiang, T. Ozaki, C.-L. Lin, C.-C. Lee, H.-C. Hsueh, and M.-C. Chung, Revealing the charge density wave caused by Peierls instability in two-dimensional $NbSe_2$, ACS Mater. Lett. **6**, 2941 (2024).

[60] P. B. Allen, Neutron spectroscopy of superconductors, Phys. Rev. B **6**, 2577 (1972).

[61] F.-H. Liu, W. Fu, Y.-H. Deng, Z.-B. Yuan, and L.-N. Wu, First-principles study of the Kohn anomaly in $TaTe_4$, Appl. Phys. Lett. **119**, 091901 (2021).

[62] C. W. Rischau, A. Korshunov, V. Multian, S. A. Lopez-Paz, C. Huang, L. Varbaro, J. Teyssier, Y. Kalcheim, S. Gariglio, A. Bosak, J.-M. Triscone, and J. del Valle, Anomalous temperature dependence of phonon lifetimes in metallic VO_2, Phys. Rev. B **109**, 094122 (2024).

[63] H. Wang, Y. Yao, F. Peng, H. Liu, and R. J. Hemley, Quantum and classical proton diffusion in superconducting clathrate hydrides, Phys. Rev. Lett. **126**, 117002 (2021).

[64] X. Gonze, S. Rostami, and C. Tantardini, Variational density functional perturbation theory for metals, Phys. Rev. B **109**, 014317 (2024).

[65] Y. Giret, A. Gellé, and B. Arnaud, Entropy driven atomic motion in laser-excited bismuth, Phys. Rev. Lett. **106**, 155503 (2011).

[66] F. Giustino, Electron-phonon interactions from first principles, Rev. Mod. Phys. **89**, 015003 (2017).

[67] X. Gonze, C. Tantardini, and A. Levitt (unpublished).

[68] R. F. W. Bader, *Atoms in Molecules: A Quantum Theory* (Clarendon, Oxford, 1990).

[69] X. Gonze, F. Jollet, F. A. Araujo, D. Adams, B. Amadon, T. Applencourt, C. Audouze, J.-M. Beuken, J. Bieder, A. Bokhanchuk, E. Bousquet, F. Bruneval, D. Caliste, M. Côté, F. Dahm, F. D. Pieve, M. Delaveau, M. D. Gennaro, B. Dorado, C. Espejo *et al.*, Recent developments in the ABINIT software package, Comput. Phys. Commun. **205**, 106 (2016).

[70] X. Gonze, B. Amadon, G. Antonius, F. Arnardi, L. Baguet, J.-M. Beuken, J. Bieder, F. Bottin, J. Bouchet, E. Bousquet, N. Brouwer, F. Bruneval, G. Brunin, T. Cavignac, J.-B. Charraud, W. Chen, M. Côté, S. Cottenier, J. Denier, G. Geneste *et al.*, The ABINIT project: Impact, environment and recent developments, Comput. Phys. Commun. **248**, 107042 (2020).

[71] A. H. Romero, D. C. Allan, B. Amadon, G. Antonius, T. Applencourt, L. Baguet, J. Bieder, F. Bottin, J. Bouchet, E. Bousquet, F. Bruneval, G. Brunin, D. Caliste, M. Côté, J. Denier, C. Dreyer, P. Ghosez, M. Giantomassi, Y. Gillet, O. Gingras *et al.*, ABINIT: Overview, and focus on selected capabilities, J. Chem. Phys. **152**, 124102 (2020).

[72] J. P. Perdew, K. Burke, and M. Ernzerhof, Generalized gradient approximation made simple, Phys. Rev. Lett. **77**, 3865 (1996).

[73] M. van Setten, M. Giantomassi, E. Bousquet, M. Verstraete, D. Hamann, X. Gonze, and G.-M. Rignanese, The pseudodojo: Training and grading a 85 element optimized norm-conserving pseudopotential table, Comput. Phys. Commun. **226**, 39 (2018).

[74] C. G. Broyden, The convergence of a class of double-rank minimization algorithms 1. General considerations, IMA J. Appl. Math. **6**, 76 (1970).

[75] D. Goldfarb, A family of variable-metric methods derived by variational means, Math. Comput. **24**, 23 (1970).

[76] D. F. Shanno, Conditioning of quasi-newton methods for function minimization, Math. Comput. **24**, 647 (1970).

[77] T. Steihaug, *Practical Methods of Optimization, Vol. 1: Unconstrained Optimization* (Wiley, New York, 1980).

[78] X. Gonze and C. Lee, Dynamical matrices, born effective charges, dielectric permittivity tensors, and interatomic force constants from density-functional perturbation theory, Phys. Rev. B **55**, 10355 (1997).

[79] C. Lee and X. Gonze, *Ab initio* calculation of the thermodynamic properties and atomic temperature factors of $SiO_2\alpha$-quartz and stishovite, Phys. Rev. B **51**, 8610 (1995).

[80] A. O. de-la Roza, M. Blanco, A. M. Pendas, and V. Luana, Critic: a new program for the topological analysis of solid-state electron densities, Comput. Phys. Commun. **180**, 157 (2009).

[81] A. O. de-la Roza, E. R. Johnson, and V. Luana, CRITIC2: A program for real-space analysis of quantum chemical interactions in solids, Comput. Phys. Commun. **185**, 1007 (2014).

[82] M. Calandra, G. Profeta, and F. Mauri, Adiabatic and nonadiabatic phonon dispersion in a Wannier function approach, Phys. Rev. B **82**, 165111 (2010).

[83] J. Berges, N. Girotto, T. Wehling, N. Marzari, and S. Poncé, Phonon self-energy corrections: To screen, or not to screen, Phys. Rev. X **13**, 041009 (2023).

[84] G. Stefanucci and E. Perfetto, Exact formula with two dynamically screened electron-phonon couplings for positive phonon-linewidths approximations, Phys. Rev. B **111**, 024307 (2025).

[85] D. R. Hamann, Optimized norm-conserving Vanderbilt pseudopotentials, Phys. Rev. B **88**, 085117 (2013).

[86] D. R. Hamann, Erratum: Optimized norm-conserving vanderbilt pseudopotentials [Phys. Rev. B **88**, 085117 (2013)], Phys. Rev. B **95**, 239906 (2017).

[87] E. v. Lenthe, E. J. Baerends, and J. G. Snijders, Relativistic regular two-component Hamiltonians, J. Chem. Phys. **99**, 4597 (1993).

[88] R. van Leeuwen, E. van Lenthe, E. J. Baerends, and J. G. Snijders, Exact solutions of regular approximate relativistic

wave equations for hydrogen-like atoms, J. Chem. Phys. **101**, 1272 (1994).

[89] E. van Lenthe, E. J. Baerends, and J. G. Snijders, Relativistic total energy using regular approximations, J. Chem. Phys. **101**, 9783 (1994).

[90] A. J. Sadlej, J. G. Snijders, E. van Lenthe, and E. J. Baerends, Four component regular relativistic Hamiltonians and the perturbational treatment of Dirac's equation, J. Chem. Phys. **102**, 1758 (1995).

[91] K. Lejaeghere, V. Van Speybroeck, G. Van Oost, and S. Cottenier, Error estimates for solid-state density-functional theory predictions: An overview by means of the ground-state elemental crystals, Crit. Rev. Solid State Mater. Sci. **39**, 1 (2014).

[92] C. Tantardini, M. Iliaš, M. Giantomassi, A. G. Kvashnin, V. Pershina, and X. Gonze, Generating and grading 34 optimised norm-conserving Vanderbilt pseudopotentials for actinides and super-heavy elements in the PSEUDODOJO, Comput. Phys. Commun. **295**, 109002 (2024).

[93] L. Komissarov, R. Rüger, M. Hellström, and T. Verstraelen, ParAMS: Parameter optimization for atomistic and molecular simulations, J. Chem. Inf. Model. **61**, 3737 (2021).

[94] A. Sommerfeld, Zur elektronentheorie der metalle auf grund der fermischen statistik, Z. Phys. **47**, 1 (1928).